



*Citation for published version:*

Jackson, R, Christodoulou, L, Li, Z, Sangan, C, Ambrose, S, Jefferson-Loveday, R, Lock, G & Scobie, J 2023, 'Influence of swirl and ingress on windage losses in a low-pressure turbine stator-well cavity', *Experiments in Fluids*, vol. 64, 173. <https://doi.org/10.1007/s00348-023-03715-7>

*DOI:*

[10.1007/s00348-023-03715-7](https://doi.org/10.1007/s00348-023-03715-7)

*Publication date:*

2023

*Document Version*

Publisher's PDF, also known as Version of record

[Link to publication](#)

*Publisher Rights*

CC BY

**University of Bath**

**Alternative formats**

If you require this document in an alternative format, please contact:  
[openaccess@bath.ac.uk](mailto:openaccess@bath.ac.uk)

**General rights**

Copyright and moral rights for the publications made accessible in the public portal are retained by the authors and/or other copyright owners and it is a condition of accessing publications that users recognise and abide by the legal requirements associated with these rights.

**Take down policy**

If you believe that this document breaches copyright please contact us providing details, and we will remove access to the work immediately and investigate your claim.



# Influence of swirl and ingress on windage losses in a low-pressure turbine stator-well cavity

Richard Jackson<sup>1</sup> · Loizos Christodoulou<sup>2</sup> · Zhihui Li<sup>2</sup> · Carl M. Sangan<sup>1</sup> · Stephen Ambrose<sup>2</sup> · Richard Jefferson-Loveday<sup>2</sup> · Gary D. Lock<sup>1</sup> · James A. Scobie<sup>1</sup>

Received: 19 January 2023 / Revised: 20 September 2023 / Accepted: 26 September 2023  
© The Author(s) 2023

## Abstract

As part of the drive towards achieving net-zero flight by 2050, the development of ultra-high bypass ratio engines will place greater importance on the efficiency of the low-pressure turbine. Stator-well cavities can be a significant source of loss within this system, primarily due to the ingestion of annulus air, which can rotate at a speed less than that of the disc. This paper presents the results of a joint experimental/numerical campaign to relate windage torque to the flow physics in a scaled, engine-realistic stator-well geometry with superposed flows. The primary variables were the pressure ratio across the stator row and the swirl ratio at inlet to the cavity. This is the first paper to relate simultaneous torque and swirl measurements in a stator-well cavity. The numerical simulations have also provided insight into the fluid dynamic behaviour. A reduction in cavity windage torque with superposed flow rate was shown, consistent with the increase in swirl measured by experiments and predicted by computations. The pre-swirled superposed flows reduce the ingestion of negatively swirling fluid from the annulus, effectively increasing the swirl ratio of the flow in the cavity towards that of the rotor. This reduces windage losses; at the design condition with superposed flow, the cavity windage torque reduced by 60% of that of the reference case. Sealing effectiveness increased with superposed flow rate. This was demonstrated through gas concentration measurement/simulations, a reduced radial flow velocity into the cavity and a reduced mass flow rate across the interstage seal. The application of a turbulent transport model showed that ingestion could be explained by shear-driven diffusion. Ingestion increased as inlet swirl ratio reduced, while the pressure ratio was found to have a negligible influence on windage moment coefficient, swirl ratio and sealing effectiveness. In addition to providing fluid dynamic insight, the gas concentration results can be used for validating thermomechanical models. The results in this paper will be of practical interest to the engine designer who wishes to scale information to engine-operating conditions.

## List of symbols

$b$	Hub radius (m)
$B$	Turbulent mixing switch-off parameter
$c$	Gas concentration (%) or chord length (m)
$C$	Absolute velocity (m/s)
$k$	Turbulent velocity scaling factor
$l_m$	Effective turbulent eddy mixing length (m)
$L_{med}$	Medial length scale (m)
$\dot{m}$	Mass flow rate (kg/s)
$M$	Windage torque (Nm)

$p$	Static pressure (Pa)
$r$	Radius (m)
$s_c$	Axial seal clearance (m)
$W$	Axial velocity (m/s)
$\rho$	Density (kg/m <sup>3</sup> )
$\mu$	Dynamic viscosity (kg/ms)
$\Omega$	Angular velocity of rotor (rad/s)

## Dimensionless parameters

$\beta$	Swirl ratio
$C_p$	Pressure coefficient
$C_M$	Moment coefficient
$\varepsilon$	Sealing effectiveness
$\lambda_T$	Turbulent flow parameter
$Ma$	Mach number
$PR$	Pressure ratio
$R_m$	Ratio of superposed flows
$Re_\phi$	Rotational Reynolds number ( $=\rho\Omega b^2/\mu$ )
$\Phi$	Sealing flow parameter

✉ James A. Scobie  
j.a.scobie@bath.ac.uk

<sup>1</sup> Turbomachinery Research Centre, Department of Mechanical Engineering, University of Bath, Bath, UK

<sup>2</sup> Gas Turbine and Transmissions Research Centre (G2TRC), Faculty of Engineering, University of Nottingham, Nottingham, UK

## Subscripts and superscripts

0	Total
1, 2, 3	Axial measurement locations
<i>a</i>	Annulus
<i>c</i>	Coolant
cav	Cavity measurement
<i>d</i>	Downstream
<i>f</i>	Across rotor fins
in	Inlet to cavity
<i>l</i>	Leakage
on	Onboarding
ref	Reference
<i>s</i>	Sample
'	Seal radius
<i>r, x, <math>\phi</math></i>	Radial, axial, tangential direction

## 1 Introduction and review of relevant research

There is currently greater need for LP turbine efficiency because the newest generation of high bypass ratio engines require a greater proportion of power for the fan, which is driven by the LP turbine. For cutting-edge ultra-high bypass ratio (UHBR) technology, the LP turbine efficiency is critical. LP turbines in UHBR engines with geared turbofans will run at much higher speeds and windage losses will therefore be more significant. For example, the Rolls-Royce Trent 700 engine has a By-Pass-Ratio (BPR) of 5:1 and an Overall Pressure Ratio (OPR) of 36:1; the UltraFan (2025) is expected to have a BPR of 15:1 and an OPR of 70:1 and promises at least 25% improvement in fuel burn relative to the Trent 700.

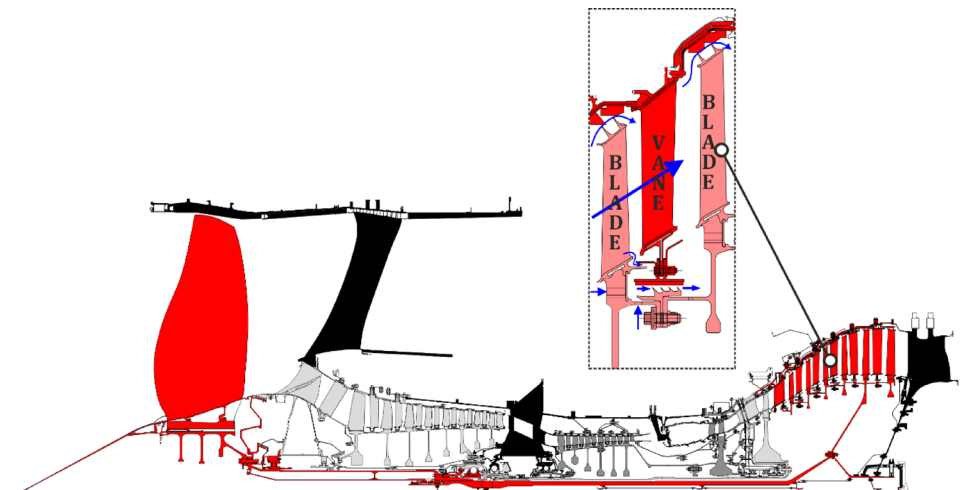
The reduction gearbox allows the fan to be driven from the LP turbine, with both at optimal rotational speeds. Therefore, an LP turbine running at a lower, fan optimised

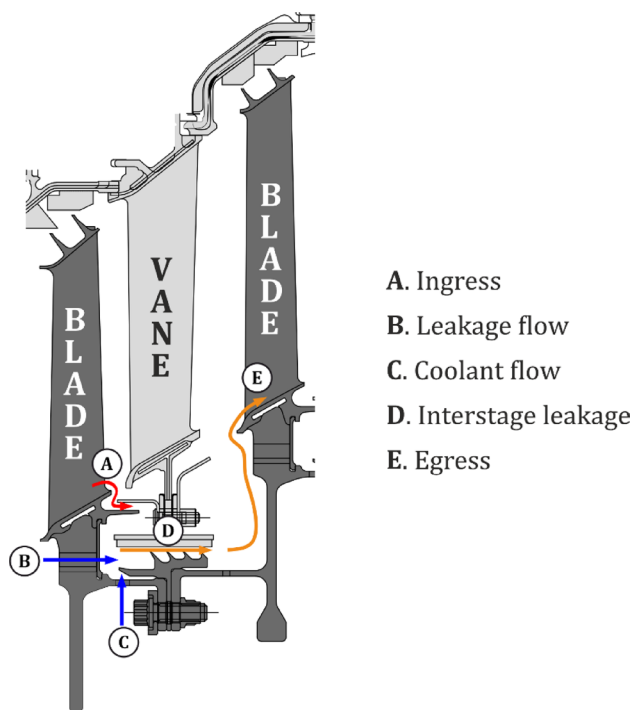
rotational speed is no longer required. For advanced future designs, LP turbine rotational speeds will increase meaning windage losses will become more significant. By running each stage closer to the optimal rotational speed the reduction gearbox allows for high OPR over fewer, smaller diameter stages, so the core is more efficient, has fewer parts and is lighter.

Figure 1 shows a cross section through a modern three-spool aero-engine with a high bypass ratio. The low-pressure (LP) system is shaded red, and the inset presents a detailed view of 1.5 stages of the LP turbine (rotor–stator–rotor) including the associated cavities. At high radius, the fin tips on the shroud of the rotor blades and the casing form a series of over-tip cavities. Mainstream annulus air can bypass the rotor stage and instead pass over the fin tips. A small radial clearance between the blade fins and an abradable lining on the casing is used to minimise this leakage.

Radially inboard of the annulus hub, a stator-well cavity is formed between two rows of rotor blades and a stator row. Figure 2 presents a detailed view of the different flow components within a stator-well cavity. Annulus air can be ingested (ingress) into the upstream wheel-space. In addition to a reduction in work output due to the bypassed flow, ingress can enter the wheel-space with a tangential velocity less than, or even opposite to, that of the rotor disc. This modifies shear stresses on the disc surface, resulting in a windage torque which acts against the direction of rotation. Teeth on the axial rotor drive-arm form a labyrinth seal with the stator foot, reducing the interstage leakage flow. The leakage flows will re-enter the annulus (“egress”) with a different incidence to that of the mainstream, which has been turned by the rotor blades or the stator vanes. This difference in flow angle will result in mixing losses. The physical mechanisms of these mixing losses are explained in detail in the literature, including the role of secondary flow structures and the implications on subsequent stages

**Fig. 1** A cross section through a modern three-spool aero-engine. The low-pressure system is shaded red. Adapted from (Fitzpatrick 2013)





**Fig. 2** Flow paths in a stator-well cavity. Adapted from (Fitzpatrick 2013)

(Hunter and Manwaring 2000; Gier et al. 2005; Schrewe et al. 2013; Guida et al. 2018; Barsi et al. 2022). The Genoa Stator-Well Cavity Rig (Guida et al. 2018; Barsi et al. 2022) features rotating cylindrical bars in the main annulus either side of the cavity to simulate rotating blades. The experimental results of Barsi et al. (2022) were used to validate a URANS simulation, which showed that the main sources of loss were at the interstage seal and the inlet and exit to the cavity. Guida et al. (2018) found that the stagnation pressure loss due to mixing at the cavity exit coincided with the location of the vane passage vortex, and that the annulus swirl ratio at inlet to the cavity influenced the stagnation pressure losses downstream. A breakdown of the contribution of each LPT cavity loss mechanism is presented by Gier et al. (2005): bypass loss, mixing loss of the re-entering flow, windage losses, step losses and subsequent-row losses. Mixing losses accounted for about 50% of all losses.

### 1.1 Superposed flows

Stator-well cavity losses can be mitigated by the addition of superposed flows. In an LPT, there are typically two: a controlled coolant flow at low radius and a leakage flow at higher radius (due to small tangential gaps between individual blades). Gas concentration experiments collected from the Sussex Stator-Well Cavity Rig show that less ingress enters the upstream wheel-space if it is purged

with superposed flow, thereby reducing any potential bypass losses (Eastwood et al. 2012; Coren et al. 2013). This finding has also been demonstrated computationally by Liu et al. (2014). As with other rotor–stator systems, the flow structure inside a stator-well cavity is dominated by regions of recirculation, with radial outflow in the boundary layer on the rotor surface due to the disc pumping effect, and inflow on the stator disc (Liu et al. 2014; Andreini et al. 2008). The flow structure in the upstream wheel-space is strongly influenced by superposed flow, but evidence suggests that the flow structure in the downstream wheel-space is weakly affected (Andreini et al. 2008; Zhang et al. 2017). Experiments and computations on the Sussex rig deduced small levels of reingestion—only 7–8% of the egress flow from the upstream wheel-space into the annulus was found to enter the downstream wheel-space as ingress (Eastwood et al. 2012; Valencia et al. 2012).

Guida et al. (2018) found that increasing the coolant flow initially reduced the stagnation pressure losses within the mixing layer at the cavity exit. However, further increasing this flow can increase the egress from the downstream wheel-space, leading to more adverse mixing with the annulus flow. This may exacerbate losses by strengthening the secondary flow structures, such as the horseshoe and passage vortices (Schrewe et al. 2013; Guida et al. 2018, Andreini et al. 2008; Liu et al. 2014).

The location, geometry and angle of the superposed flow feeds can strongly influence the sealing effectiveness. Simulations on the Sussex Rig by Andreini et al. (2011) showed that ingress into the upstream wheel-space can be reduced by positioning the flow feed further upstream on the axial rotor drive arm and angled towards the rotor. It was found that the coolant flow is entrained in the rotor boundary layer, which acted as a barrier to ingestion. These simulations were validated by experiments, which used temperature measurements to identify the flow paths (Coren et al. 2011). Zhang et al. (2017) showed that the geometry and radial location of the coolant flow feed (on the radial surface of the rotor) influenced the flow characteristics and sealing effectiveness in the upstream wheel-space. The influence in the downstream cavity was shown to be minor and the sealing effectiveness was virtually invariant with radius.

There is substantial evidence in the literature on the mixing loss mechanisms between the cavity egress and the main annulus flow; however, evidence on the windage loss mechanisms *within* the cavity is limited. This paper presents the results of a combined computational and experimental study that relates the windage losses with the fluid dynamics within a stator-well cavity, when subjected to varying flow conditions (i.e. inlet swirl ratio, pressure ratio and superposed flow rate). An understanding of the main sources of windage loss will allow for careful design of flow control devices, which can be used to minimise this loss. The design

and measurement of the impact of flow control devices are described in associated papers (Li et al. 2023, Jackson et al. 2023).

## 2 Experimental facility

Experiments were conducted using a cold flow axial turbine rig at the University of Bath. Figure 3a presents a sliced view of the rig test section, showing the *cavity*, the main gas path, the superposed flows (leakage and coolant) and the axial measurement stations (1,2,3). The test facility was deliberately designed to operate without rotor blades, with the vane geometry forming an engine representative range of swirl ratio to simulate that generated by a rotor. As discussed in Sect. 2.2, the radial distribution of swirl was the primary parameter characterising the fluid dynamics. The experiments modelled a stator-well cavity to assess the ingress and windage losses in an engine-representative environment at low TRL. Axial station 1 is at the inlet to the test section, while stations 2 and 3 are at the mid-gap of the upstream and downstream cavity entrances, respectively. A detailed view of the flow paths and velocity

components in the stationary frame of reference is presented in Fig. 3b. Here, the numeric labelling corresponds with the same features as in Fig. 2. The contracting annulus and the two rows of prismatic (2-dimensional) vanes were designed to generate the required annulus swirl ( $\beta_{in}$ ) and static pressure ratio (PR) conditions across the second stator row, where

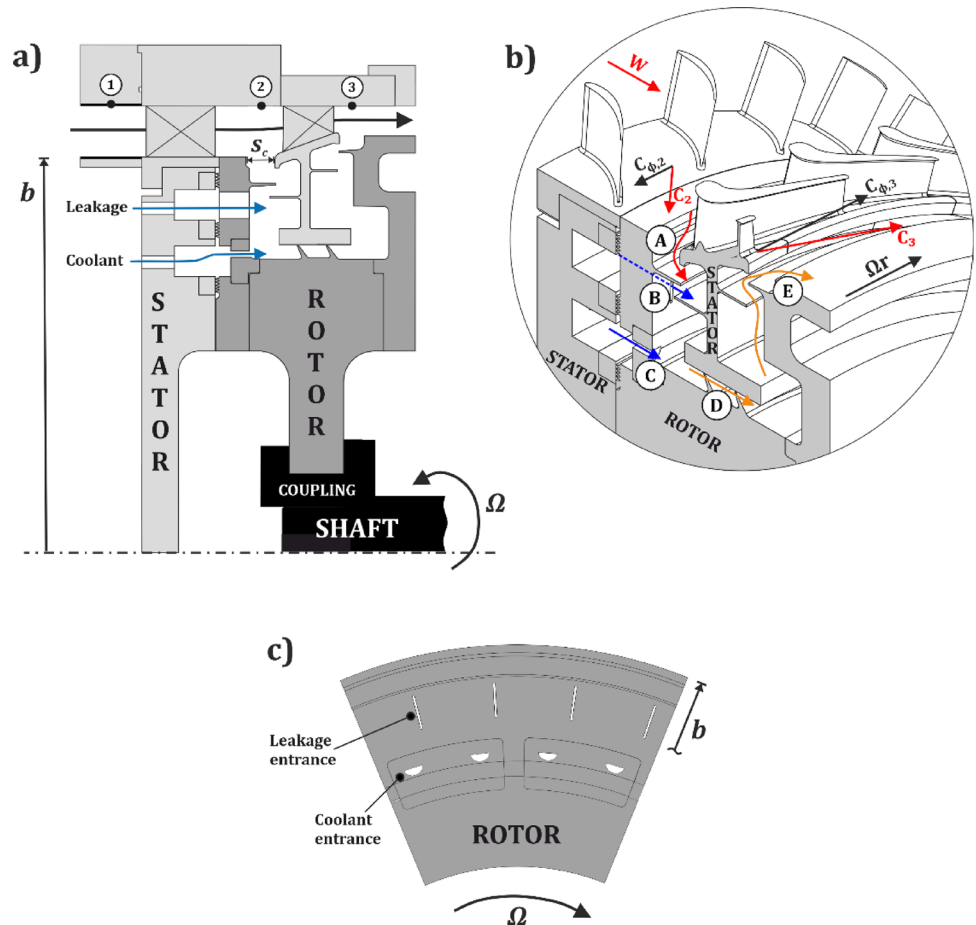
$$\beta_{in} = \frac{C_{\phi,2}}{\Omega b} \tag{1}$$

$$PR = \frac{p_2}{p_3} \tag{2}$$

The annulus flow was delivered by a screw blower. The flow temperature immediately upstream of the inlet guide vanes was regulated to approximately 25 °C by two water-cooled heat exchangers.

A three-part aluminium bladeless rotor was used to form the rotating surfaces of the stator-well cavity. The rotor was spun by a 34 kW dynamometer, achieving a maximum rotational Reynolds number of  $Re_{\phi} = 1.2 \times 10^6$ . The

**Fig. 3** The test section, showing **a** the main components, **b** the flow paths and velocity components in the stationary frame of reference, and **c** the superposed flow geometries at the entrance to the cavity



drivetrain included a flexible coupling, a pair of grease-filled deep groove ball bearings, and a torque meter—the details of which are described in the following section.

The first stator row was machined out of aluminium, while the second stator row was formed of vane doublets that were printed using stereolithography (SLA) out of a solid material with ABS/polypropylene characteristics. Additive manufacturing was used due to the complexity of the geometry, the inclusion of small pressure taps, and because a subsequent phase of the research is to measure the windage reduction of different flow control concepts. The build direction was determined by the best compromise between surface finish, small feature definition and consistent and predictable manufacture. The minimum thickness printed was 0.2 mm.

Superposed flows that modelled the leakage and coolant paths were supplied via two separate feed lines. Each superposed flow path was isolated from the other by labyrinth seals, formed by sets of teeth on the rotor face, which aligned with an abradable material (Tufnol) on the stator surface opposite. The flow settled in plenum chambers, before passing through the rotor into the cavity, via entrance feeds—the geometries of which are shown in Fig. 3c. The leakage flow passed through narrow radial slots, which modelled the small gaps between blades. The coolant flow entered through semi-elliptical slots, which had an angular offset from the leakage slots, replicating engine conditions. The annulus and superposed flow rates were measured by thermal mass flow meters to within 1% of the full-scale range.

The superposed flow rates can be presented non-dimensionally by the sealing flow parameter,  $\Phi_0$ , which combines the effects of the sealing mass flow and disc rotation.

$$\Phi = \frac{\dot{m}}{2\pi s_c \rho \Omega b^2} \tag{3a}$$

The total superposed flow is equivalent to the sum of the leakage and coolant flows:

$$\Phi_0 = \Phi_l + \Phi_c \tag{3b}$$

$$\Phi_l = \frac{\dot{m}_l}{2\pi s_c \rho \Omega b^2} \tag{3c}$$

$$\Phi_c = \frac{\dot{m}_c}{2\pi s_c \rho \Omega b^2} \tag{3d}$$

The ratio of the superposed flows is defined as follows:

$$R_{\dot{m}} = \frac{\Phi_l}{\Phi_c} \tag{4}$$

The flow structure in the wheel-space is governed by the turbulent flow parameter,  $\lambda_T$ :

$$\lambda_T = \frac{\dot{m}}{\mu b} \text{Re}_\phi^{-0.8} \tag{5}$$

For the free disc, where there is no stator, the entrained flow rate is characterised by  $\lambda_T \approx 0.22$ . The origin of this is the modelling approach by von Kármán (Kármán and von. 1921). It follows from Eqs. (5, 3a) that  $\lambda_T = 2\pi G_c \text{Re}_\phi^{0.2} \Phi_0$ , where  $G_c = s_c/b$  is the gap ratio. It is well established that the structure of the flow in the wheel-space is determined by the turbulent flow parameter (governing a viscous phenomenon),  $\lambda_T$  and only weakly dependent on rotational Reynolds number (Owen and Rogers 1989).

Table 1 lists the range of the salient operating parameters of the rig.

### 2.1 Torque measurement

The windage torque was measured by an in-line torque meter (HBM T12), which was mounted in the drivetrain between the dynamometer and flexible coupling (as shown in Fig. 4), and which was calibrated in situ over the measurement range. The torque was acquired at a sampling rate of 80 Hz through a 1 Hz low-pass filter. For each flow condition, the data were sampled and averaged with a median filter over a 120 s period. The measured windage torque ( $M$ , denoted as positive against the direction of rotation) includes losses other than the cavity windage (e.g. friction in the bearings and on the external disc surfaces). Therefore,  $M$  is expressed relative to a reference case ( $M_{\text{ref}}$ ), which is defined to be the torque at a given PR and  $\beta_{\text{in}}$  condition with no superposed flow ( $\lambda_T = 0$ ). The result is expressed non-dimensionally as a change in moment coefficient on the reference case ( $\Delta C_M$ ):

$$\Delta C_M = \frac{M - M_{\text{ref}} - M_{\text{on}}}{1/2 \rho \Omega^2 b^5} \tag{6}$$

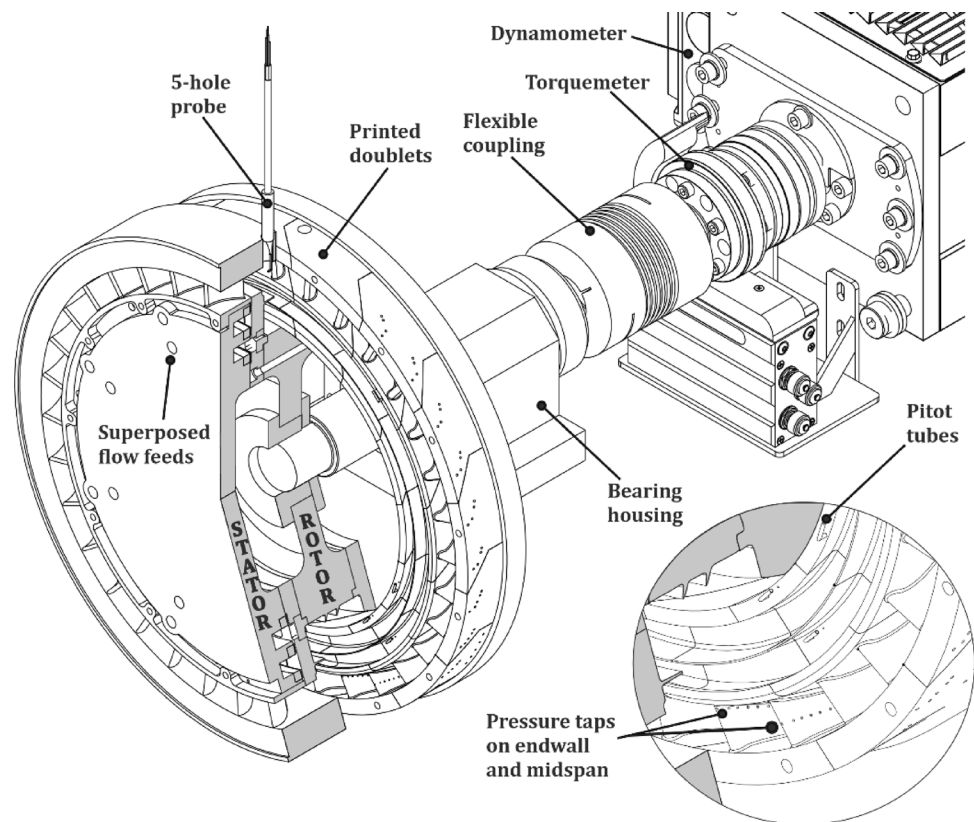
$M_{\text{on}}$  is the onboarding torque of the superposed flow, as it is rotationally accelerated to the disc speed when it passes

**Table 1** Test rig operating conditions

Parameter	Range	Design condition
$\text{Re}_\phi$	$0.4 \times 10^6 \rightarrow 1.2 \times 10^6$	$1.2 \times 10^6$
$\beta_{\text{in}}$	$-0.1 \rightarrow -0.6$	$-0.27$
PR	$1.1 \rightarrow 1.24$	1.24
$\Phi_0$	$0 \rightarrow 0.07$	0.038
$R_{\dot{m}}$	$0 \rightarrow \infty$	0.73
$\lambda_T$	$0 \rightarrow 0.5$	0.29



**Fig. 4** An isometric view of the test section and instrumentation



through the rotor, into the cavity. This is calculated analytically as follows:

$$M_{\text{on}} = \Omega(\dot{m}_c r_c^2 + \dot{m}_l r_l^2) \quad (7)$$

Since bearing torque losses are a strong function of the grease viscosity (and hence temperature), the system underwent a carefully designed warm-up procedure. This ensured that the losses were repeatable for experiments performed at the same PR and  $\beta_{\text{in}}$  conditions. The temperature of the bearing housing was monitored with a *K* type thermocouple, to ensure that the same steady state temperature was achieved for each set of conditions (to within  $\pm 1$  °C). This procedure resulted in a repeatability of the torque measurement (including on different days and after re-builds) to be within  $\pm 10.02$  Nm. An example torque trace is presented in Appendix 1.

## 2.2 Pressure and swirl measurement

Static pressure measurements in the cavity were collected via radially distributed surface taps on the printed doublets in the upstream and downstream wheel-spaces. These were paired with total pressures that were measured at the same radial coordinates using pitot tubes angled tangentially to the local radial direction (see inset of Fig. 4). Each static/total pressure pair was used to calculate a local tangential

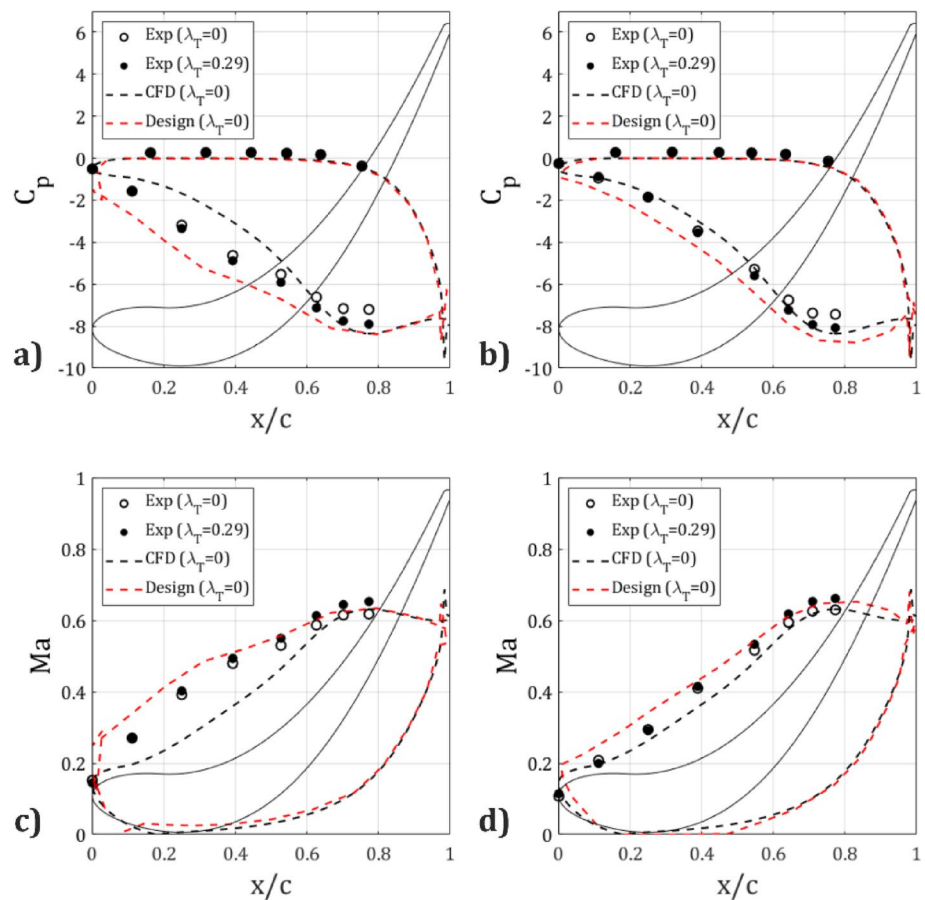
component of velocity. Since the direction of tangential velocity could depend upon  $\beta_{\text{in}}$ , a mirrored set of static and total pressure taps were included, where the direction of the pitot was reversed. Five static pressure taps were distributed in the annulus across one vane pitch, upstream and downstream of the second stator row (at axial stations 2 and 3). The pitch-averaged pressures were used to calculate PR.

Pressure taps were also distributed around a pair of vanes (see inset of Fig. 4). One set were close to the end-wall (at a fixed distance from the rising hub surface of 8% of the full-span) and the second were along the mid-span. The measured vane pressures are shown in Fig. 5a, b for the mid-span and endwall, respectively. They are shown for both the reference case ( $\lambda_T = 0$ ) and the design case ( $\lambda_T = 0.29$ ). Also shown are the CFD predictions and the design requirements (both for the reference case). The results are presented as a pressure coefficient ( $C_p$ ), which is defined as follows:

$$C_p = \frac{p - p_2}{1/2 \rho \Omega^2 b^2} \quad (8)$$

The absolute static pressures on the vane and at axial station 2 are  $p$  and  $p_2$ , respectively. The suction surface of the vane is generating a larger magnitude of  $C_p$

**Fig. 5** Vane pressure distribution at **a** the mid-span and **b** the endwall. Isentropic Mach number distributions at **c** the mid-span and **d** the endwall



at the mid-span than the endwall over the axial range  $0 < x/c < 0.6$ . This is likely caused by endwall losses from secondary flow structures. The measurements match closely to the design requirements and are in qualitative agreement with the computations. Figure 5c, d presents the isentropic Mach numbers at the two spanwise locations. This is defined as follows:

$$Ma = \sqrt{\left( \left( \frac{P_{0,2}}{P} \right)^{\frac{\gamma-1}{\gamma}} - 1 \right) \frac{2}{\gamma-1}} \tag{9}$$

Since  $Ma$  is coupled to the local static pressure, the trends for the isentropic Mach number are similar to those for  $C_p$ . The larger  $C_p$  magnitude at the mid-span ( $0 < x/c < 0.6$ ) causes a higher  $Ma$ . The isentropic Mach number reaches a maximum of  $Ma = 0.6$  at  $x/c = 0.75$ .

Gauge pressures were measured using four differential transducers (ESI PR3202) that were individually calibrated in-house. Each transducer was connected to a 48-channel Scani-valve system, allowing up to 192 pressure measurements to be made during a single experiment. The pressure data were acquired at 80 Hz and averaged over 2 s, following a settling period of a further 2 s.

The local velocity components and corresponding angles of the flow upstream and downstream of the stator (at axial stations 2 and 3) were determined using pressure measurements from a custom drilled-elbow five-hole probe (manufactured by Vectoflow GmbH). The probe had a head diameter of 1.5 mm. The radial coordinate of the probe was controlled using a bespoke traversing system. Five separate differential transducers (“All Sensors” 5PSI-D-PRIME-MV, 345 mbar range) simultaneously acquired the pressures, sampled at 100 Hz over a 2 s period before being averaged. Flow angles and velocities were then derived by applying the data to calibration coefficients. These coefficients were provided by Vectoflow, following their in-house calibration of the probe.

### 2.3 Ingestion measurement

The ingestion of annulus air into the cavity was quantified using a gas concentration measurement technique.  $CO_2$  could be seeded at a known concentration into either (or both) superposed flow paths ( $c_1 = c_c \sim 0.5\text{--}1\%$ ). Static and total pressure taps on the stator wall were used to measure a sample concentration ( $c_s$ ) at different locations within the cavity. A pump delivered the sample gas to a Signal Group



9000MGA infrared gas analyser, which had a repeatability of  $\pm 1\%$  of the full-scale range. Up to 20 different samples were measured in each experiment using a multiplexer. Concentration samples were averaged over a 10 s period, following stabilisation.

The sealing effectiveness ( $\varepsilon_c$ ) was calculated using the sample ( $c_s$ ), annulus ( $c_a$ ) and superposed flow concentrations ( $c_0 = c_l = c_c$ ):

$$\varepsilon_c = \frac{c_s - c_a}{c_0 - c_a} \quad (10)$$

Therefore, when  $\varepsilon_c = 1$ , the cavity is fully sealed. The annulus concentration ( $c_a$ ) was monitored upstream of the inlet guide vane.

### 3 Numerical model

The University of Nottingham performed CFD simulations using a compressible URANS solver in ANSYS Fluent v2021R1. This is based on a finite volume approach and used second-order upwinding for discretisation of momentum terms and the Menter SST turbulence model. A dual time stepping method was used, with 50 main iterations required per blade passing period and 40 sub-iterations for the inner loops at each main iteration. The time step size was set to  $1.0 \times 10^{-5}$  s. The CFL number was  $\sim 1$ . Boundary conditions were informed from experimental measurements. The measured total temperature and pressure were specified at the main annulus inlet plane, with an appropriate radial pressure gradient at the outlet plane. At the secondary flow inlets, mass flow rates were specified based on experimentally measured values. The domain consisted of a 1:1 ratio

of inlet guide vane to secondary vane for a single blade passage.

Meshes were generated using ANSYS/TurboGrid and ANSYS/ICEM, the former for the main passage and the latter for the hub. Figure 6 presents a figure of the generated mesh. Note the vectors appear non-uniform because the background cross section is a curved surface, not a plane. Approximately 84% of the total grid count accounted for the annulus and cavity domains and used hexahedral meshing and the coolant feeds used tetrahedral elements. At the first off-wall grid node  $y^+ \sim 1$  in the main annulus and cavity zones. The Enhanced Wall Treatment was deployed to extend the applicability of the wall function through the wall near-wall region. The wall function blending the linear and logarithmic law (Kader 1981) was applied in the  $K$  Omega SST turbulence model, providing velocity profiles in the region  $y^+ \sim 10$ . Following mesh independence studies, a final mesh with  $10^7$  cells was selected.

Approximately 64,000 core hours were required for each simulation. At each time step, sub-iterations were performed until residuals achieved a magnitude of  $10^{-6}$  or less. Around six cavity revolutions were required to achieve a stable windage torque which was defined to have converged when the relative change in mean torque between each revolution was less than 5%.

### 4 Influence of superposed flows on fluid structures and windage loss

The swirl flow field is presented in Fig. 7a for the reference case with no superposed flow ( $PR = 1.24$ ;  $\beta_{in} = -0.27$ ;  $\lambda_T = 0$ ). The central cavity silhouette includes the radial location of the pressure measurements (black filled circles). Swirl data from the upstream and downstream wheel-spaces

**Fig. 6** Mesh of the numerical domain

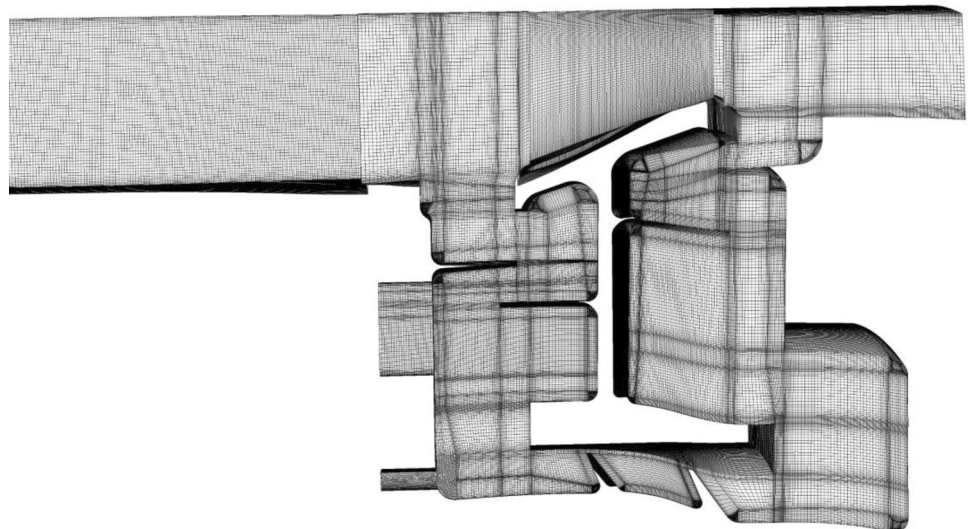
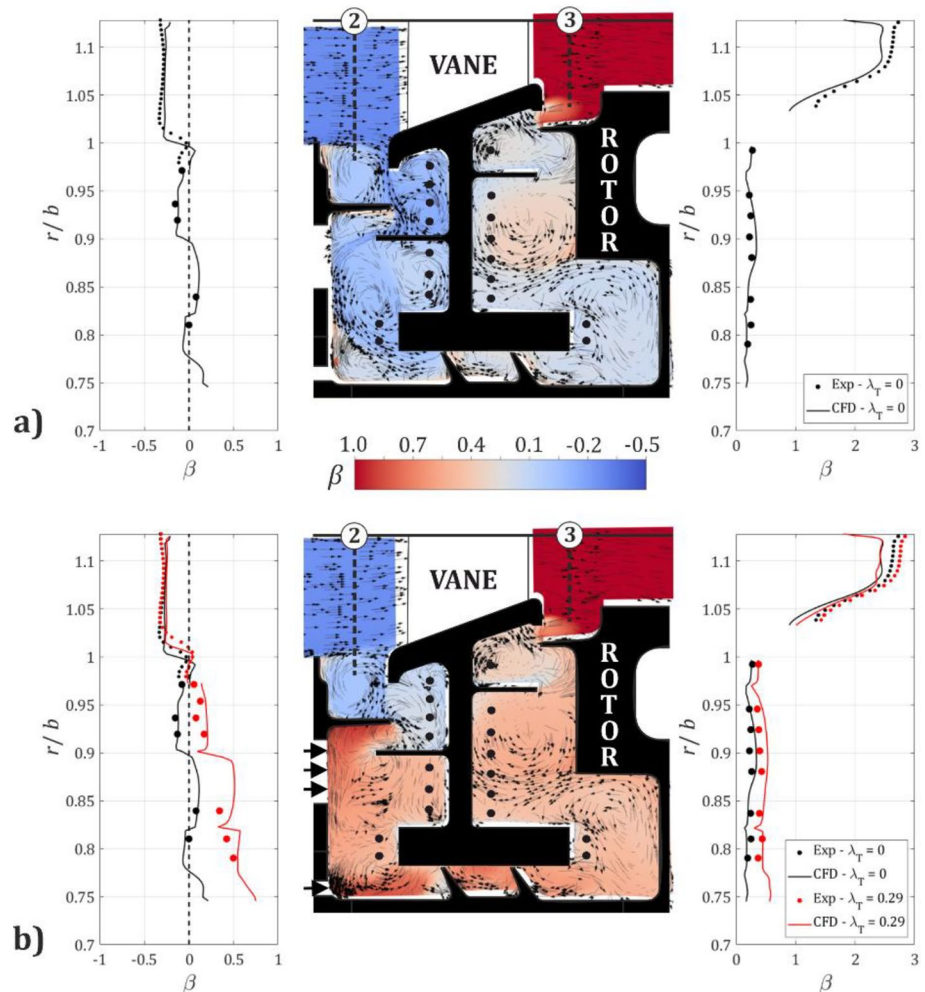


**Fig. 7** Swirl ratio flow field (PR = 1.24;  $\beta_{in} = -0.27$ ;  $Re\Phi = 1.2 \times 10^6$ ). **a** No superposed flow ( $\lambda_T = 0$ ). **b** Design condition ( $\lambda_T = 0.29$ )



are presented to the left and right of the cavity silhouette, respectively. The experimental data points are radially aligned with the measurement locations. The annulus swirl data (from the five-hole probe) are shown by the smaller data points and the corresponding traverse lines in the central figure. Velocity vectors and contours of the time-averaged swirl from the computations are overlaid on the silhouette. Radial lines of computed swirl are extracted at the same axial coordinates as the measurements, for comparison. Note that the radial line of computed swirl in the downstream annulus has been extracted at the same pitch wise coordinate as the five-hole probe. The swirl has not been averaged across a vane pitch, due to the proximity of the stator vanes immediately upstream.

Consider the path of the annulus flow that bypasses the vane in Fig. 7a. The flow upstream of the vane approaches with negative swirl, which is broadly constant across the radius of the annulus ( $\beta_{in} \sim -0.27$  for both experiments and computations). Some flow is ingested into the upstream wheel-space, as demonstrated by the computed velocity vectors. The ingestion is restricted to the stator surface by

a region of recirculation, which has a slightly higher swirl due to the proximity of the rotor surface. This increase in swirl is consistent with the measurements from the five-hole probe. As the ingestion flows radially inward of the axial fins, its path is determined by pairs of counter-rotating vortices, guiding it close to the rotor surface. The influence of the rotating disc surface at low radius causes  $\beta > 0$ . This positively swirling flow passes through the interstage seal to the downstream wheel-space, where the measured swirl is virtually invariant with radius. There is further good agreement between the measured and computed swirl. Experiments and computations both show a radial increase in swirl at the exit from the downstream wheel-space as the egress mixes with highly swirling flow from the vane.

The addition of superposed flow ( $\lambda_T = 0.29$ ) through the leakage and coolant feeds causes an increase in the measured and computed swirl in the upstream wheel-space (see Fig. 7b). As the superposed flows enter the cavity at the disc rotational speed, this increases the swirl of the cavity flow, most noticeably inboard of the axial stator fin. Here, the counter-rotating vortex pair previously seen in the

baseline case (Fig. 7a) has been modified. There is a moderate increase in swirl outboard of the stator fin, which is also detected by the five-hole probe at the cavity inlet. The computed vectors suggest that the ingestion from the annulus has reduced, which is later confirmed by the gas concentration results in Sect. 5. The high swirl at low radius is carried over to the downstream wheel-space, where the vectors suggest that the flow structure is unchanged. This is consistent with computational findings by Andreini et al. (2008) and Zhang et al. (2017) who show that superposed flow entering the upstream wheel-space of a stator-well cavity has little influence on the behaviour in the downstream wheel-space. As with the baseline case, there is good qualitative agreement between the experimental swirl measurements and the computations. There is a small, measured increase in swirl downstream of the vane. This is likely a result of more mass flow passing over the annulus due to reduced ingestion.

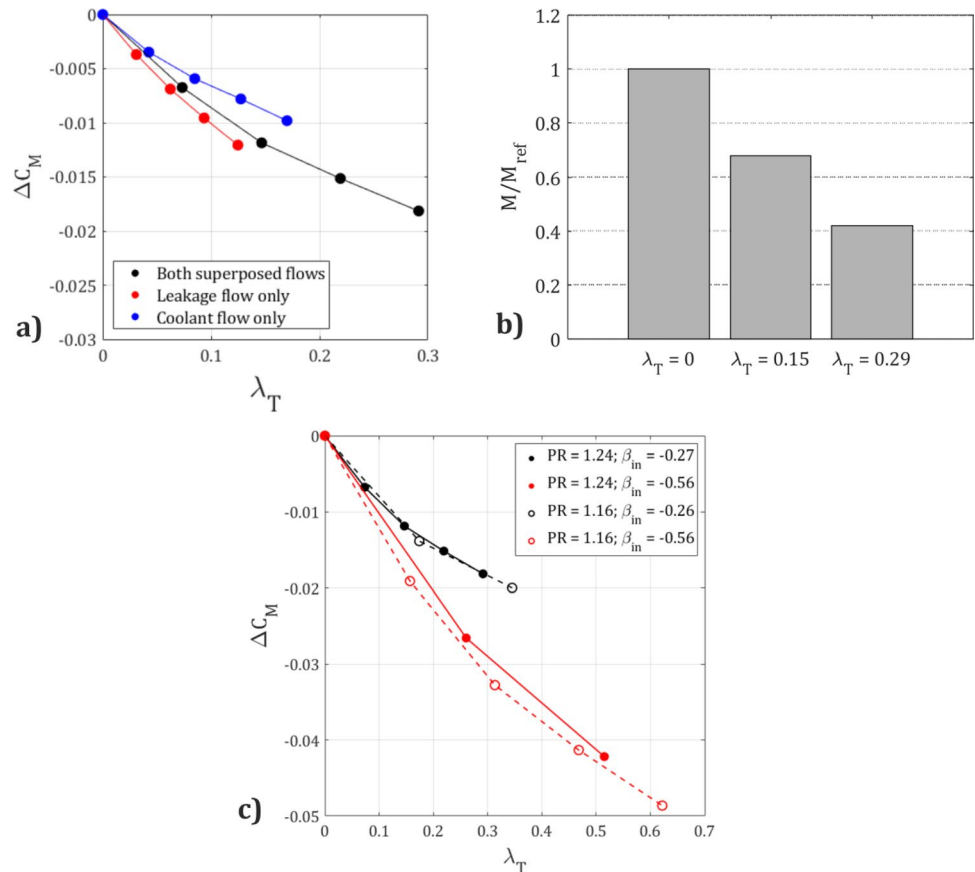
Figure 8a presents the measured change in moment coefficient ( $\Delta C_M$ ) with non-dimensional superposed flow rate ( $\lambda_T$ ), for three different scenarios: i) both superposed flows with a fixed relative fraction ( $R_{in} = 0.73$ ) ii) leakage flow only and iii) coolant flow only. The change is relative to the torque for the reference case ( $\lambda_T = 0$ ). The appropriate onboarding torque element ( $M_{on}$ ) has been considered in the calculation of  $\Delta C_M$ , in accordance with Eqs. 6 and 7. Figure 8a shows

that, for a given  $\lambda_T$ , the leakage flow provides a greater contribution to the overall torque reduction.

The change in windage torque is shown as a fraction of  $M_{ref}$  in Fig. 8b. The computed windage torque comes from integrating the time-averaged shear stresses on the internal rotating surfaces of the cavity. A direct comparison between the computed and measured windage torque was not performed since the experiment contains additional windage torque contributions from the drivetrain, which was not modelled in the CFD. Figure 8b shows that the computed cavity torque at the design condition ( $\lambda_T = 0.29$ ) is approximately 60% less than the reference case ( $\lambda_T = 0$ ).

The influence of  $\lambda_T$  on  $\Delta C_M$  is presented in Fig. 8c, for two conditions of  $\beta_{in}$  and PR ( $R_{in} = 0.73$ ). It shows that at an annulus flow condition with a more negative  $\beta_{in}$ , an equivalent  $\lambda_T$  causes the windage moment coefficient to reduce further. Since  $\beta_{in}$  directly influences the cavity swirl, which in turn influences the shear stresses and windage, there is a greater potential to reduce the windage moment coefficient if the cavity swirl is more negative. There is a negligible effect of PR.

**Fig. 8** Influence of  $\lambda_T$  on windage torque: **a** measured  $\Delta C_M$  **b** computed relative change in windage torque and **c** influence of PR and  $\beta_{in}$



### 5 Cavity sealing effectiveness

The following section describes the results of gas concentration measurements and computations, which were used to determine the sealing effectiveness ( $\epsilon_c$ ) of the stator-well cavity. In these experiments, the coolant and leakage flows were seeded with a tracer gas concentration of  $\sim 1\%$  CO<sub>2</sub>. The higher the value of  $\epsilon_c$ , the lower the quantity of ingested annulus air. The inverse of the sealing effectiveness can be thought of as a “bypass loss” (as termed by Gier et al. 2005).

Figure 9 presents the experimental measurements and computational results of  $\epsilon_c$  at the design condition (PR = 1.24;  $\beta_{in} = -0.27$ ;  $\lambda_T = 0.29$ ). Computed values of  $\epsilon_c$  are shown by the central contour plot. Radial distributions of  $\epsilon_c$  in the upstream and downstream wheel-spaces are presented in the graphs to the left and right of the cavity, respectively. The downstream sealing effectiveness is also presented as  $\epsilon_{c,d}$ , where  $c_0$  is the concentration immediately upstream of the interstage seal. The symbols refer to measurements taken on the wall (filled circles) and in the core, 5 mm from the surface (open diamonds). These measurement locations are radially aligned with those on the central silhouette. The red lines correspond to the computed  $\epsilon_c$ , which were extracted adjacent to the stator surface. The five-hole probe was used to measure gas concentration radially along the mid-gap of the downstream wheel-space. (No equivalent upstream measurements are presented due to indeterminate levels of gas concentration).

In the upstream wheel-space,  $\epsilon_c$  reduces with radius, signifying that ingestion from the annulus flow is primarily limited to the outer radius by the superposed flows. The

step reduction in  $\epsilon_c$  across the axial stator fin demonstrates that this feature is effective at preventing ingress from entering the inner part of the wheel-space. Very low  $\epsilon_c$  at high radius signifies that the flow is dominated by ingestion.  $\epsilon_c$  at the core and wall are almost equal, which suggests that the flow is fully mixed. The experimental results are in good qualitative agreement with the computations.

The downstream wheel-space is comparable to a simple stator-rotor system with a low-radius bore flow. As is also the case with such systems, Fig. 9 shows that for  $r/b < 1$  (inboard of the axial rotor fin),  $\epsilon_c$  is virtually invariant with radius. This suggests near-complete mixing of the flow near to the axial rotor fin. Since there is no apparent radial change in  $\epsilon_c$  across the stator fin, this feature has limited sealing efficacy.  $\epsilon_c$  gradually reduces outboard of the rotor fin, due to mixing of the cavity and annulus flows. As with the upstream wheel-space,  $\epsilon_c$  in the core and adjacent to the wall are near-identical, indicating that the flow is fully mixed. Low levels of ingress into the downstream wheel-space are demonstrated by high  $\epsilon_{c,d}$ . Reingestion from the upstream wheel-space was deemed to be negligible since indeterminate gas concentration was measured on the vane end-wall static pressure taps (the locations of which are shown in the inset of Fig. 4).

The contribution of each superposed flow path to  $\epsilon_c$  can be quantified by seeding each flow in turn. Figure 10 shows the separate contributions for the stator wall effectiveness measurements. The effectiveness distributions of the separately seeded leakage and coolant flows are consistent with the radial positions at which they enter the cavity. Outboard of the upstream stator axial fin, the sealing contribution is greater from the leakage flow. Immediately inboard of the fin, the contribution of both flows is similar, but at low radius, the effect of the coolant flow is more significant. As

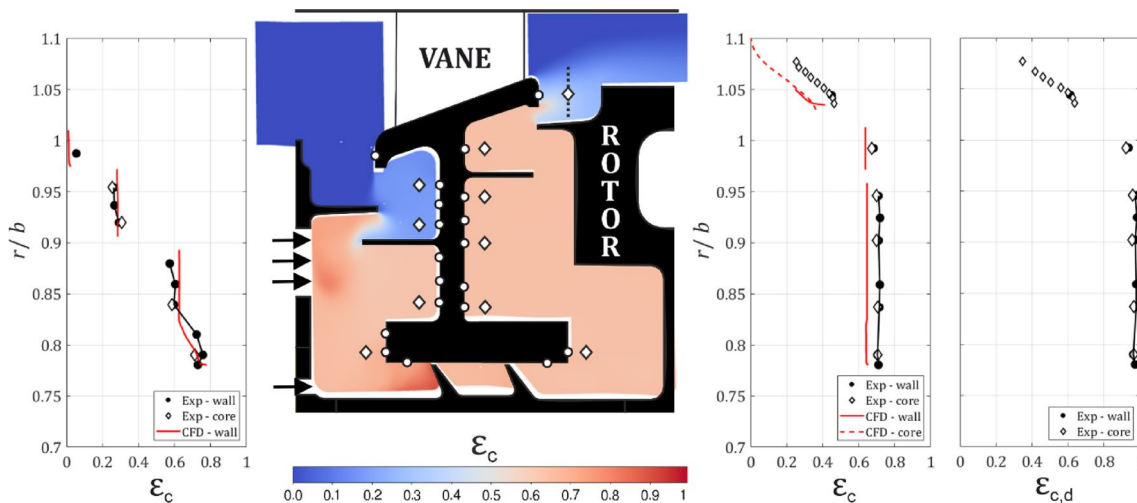
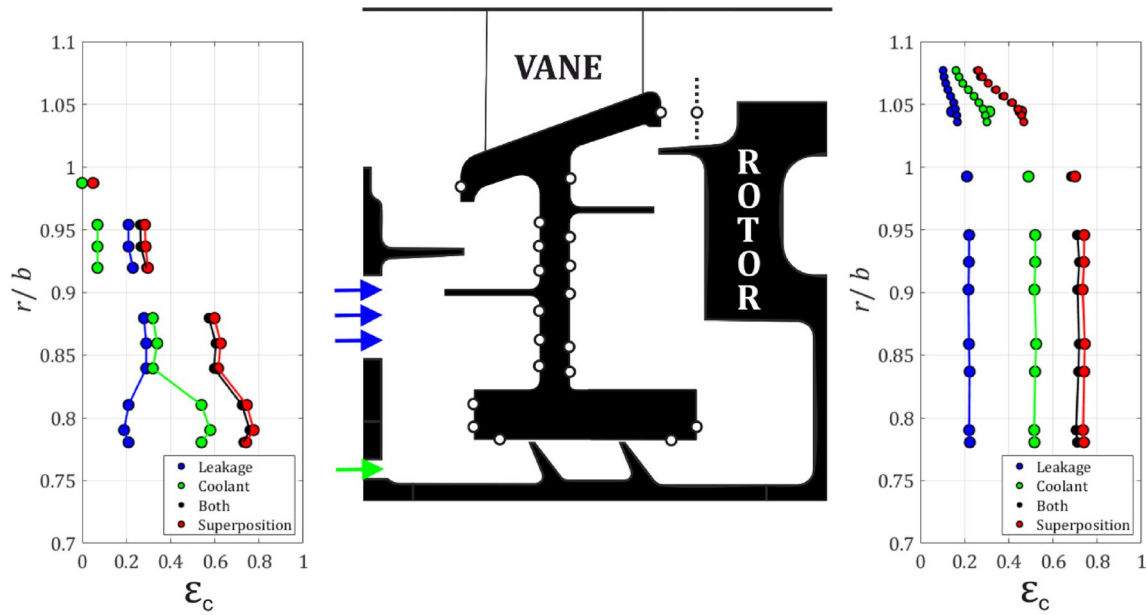


Fig. 9 Sealing effectiveness at design condition (PR = 1.24;  $\beta_{in} = -0.27$ ;  $Re\Phi = 1.2 \times 10^6$ ;  $\Phi_0 = 0.038$ )





**Fig. 10** Individual superposed flow path contribution to  $\epsilon_c$  at design condition ( $PR = 1.24$ ;  $\beta_{in} = -0.27$ ;  $Re_\Phi = 1.2 \times 10^6$ ;  $\Phi_0 = 0.038$ )

a means of validating the measurements, the superposition of  $\epsilon_c$  from the individually seeded flows are presented. This distribution is virtually equal to the  $\epsilon_c$  when seeding both flows simultaneously.

In the downstream wheel-space, the relative  $\epsilon_c$  contributions from the individual superposed flows are broadly invariant with radius until  $r/b \sim 1$ . The trend follows a similar behaviour to the case with both flows seeded. For this case,  $\epsilon_c$  is almost equal to the superposition of the results from the individually seeded flows. For all cases,  $\epsilon_c$  in the downstream cavity ( $r/b < 1$ ) is virtually equal to the effectiveness immediately upstream of the interstage seal, indicating low levels of ingestion.

Figure 11 shows the effect of superposed flow rate on sealing effectiveness, measured at a location in the downstream wheel-space, indicated on the inset figure. In order to increase the accessible range of  $\lambda_T$ , the pressure ratio was reduced to  $PR = 1.10$  ( $Re_\Phi = 0.6 \times 10^6$ ). Figure 11 shows that the effectiveness (and therefore flow field) is independent of  $Re_\Phi$ . With increasing  $\lambda_T$ , the sealing effectiveness with both flows tends to  $\epsilon_c = 1$ . The coolant flow contribution towards  $\epsilon_c$  is more significant since more of this flow passes over the interstage seal. As with the results in Fig. 10, the summation of  $\epsilon_c$  for the individual flows is comparable with that for both flows seeded simultaneously.

Since  $\epsilon_c$  is independent of  $Re_\Phi$ , the measurements presented in Figs. 9, 10 can be scaled to engine conditions and used to validate thermomechanical models that predict disc metal temperatures.

The variation of sealing effectiveness with inlet swirl ratio is shown in Fig. 12, for the measurement location in

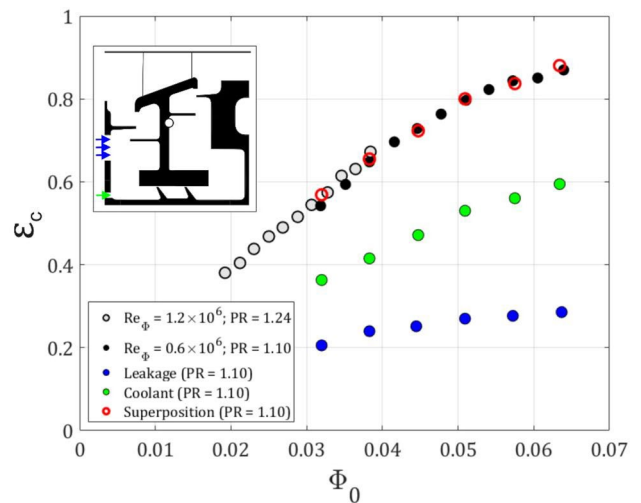


**Fig. 11** Variation of  $\epsilon_c$  with  $\Phi_0$  ( $\beta_{in} = -0.27$ ; "R" "m" = 0.73)

the upstream wheel-space indicated in the inset figure. The results for two  $\Phi_0$  are shown. As  $\beta_{in}$  tends to zero, the effectiveness increases and the cavity becomes better sealed. The concept, and measured evidence of the changes in ingestion with varying mismatch velocity and shear layer activity, was first published by Savov et al. (2017). An ingress model that was developed by Savov and Atkins (2017) (including evidence of the changes in ingestion with varying shear-layer activity) has been fitted to this data. The model is underpinned by turbulent transport theory and the mixing length hypothesis. An explicit form of the model was later derived by Graikos et al. (2022):



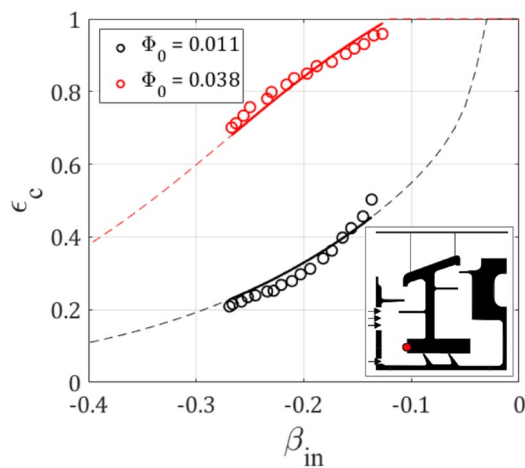


**Fig. 12** Effect of inlet swirl ratio on measured sealing effectiveness. (Symbols represent experimental data and lines theoretical fits) ( $Re\Phi = 1.2 \times 10^6$ ; "R" "\_" "m" = 0.73)

$$\epsilon_c = \frac{-\Phi_0^2 + \sqrt{\Phi_0^4 + 4\Phi_0^2 \left(\frac{kl_m}{L_{med}}\right) (1 - B\Phi_0)}}{2 \left(\frac{kl_m}{L_{med}}\right) (1 - B\Phi_0)} \quad (11)$$

The reader is encouraged to refer to Savov and Atkins (2017); Graikos et al. 2022) for more details on the individual parameters.  $L_{med}$  is the medial length of the seal and  $B$  is an aggregated function which considers geometric properties of the seal, the density ratio and flow coefficient. The mixing length,  $l_m$ , is an empirical parameter, but one which is primarily a function of the difference between  $\beta_{in}$  and a local swirl inboard of the seal,  $\beta_{cav}$ .

$$\frac{l_m}{b} = A_1 \exp(A_2 |\beta_{in} - \beta_{cav}|) \quad (12)$$

Therefore, the larger the difference between the annulus swirl and the local cavity swirl, the larger the mixing length due to the stronger shear effects. This in turn will cause stronger mixing, resulting in an increase in ingestion. For the results of the model presented in Fig. 12,  $\beta_{cav} = 0.49$ . This is based upon the local swirl measured at the same location as the gas concentration (filled red circle on Fig. 12 inset) for the case where  $\beta_{in} = -0.27$ .

The increased sealing performance with superposed flow can also be demonstrated through inference of the net ingestion into the upstream wheel-space. The interstage leakage flow rate was calibrated with pressure drop (see Appendix 2 for further details). The net ingestion (labelled (1) in Fig. 13a) was then calculated by subtracting the superposed

flow rate (3) from the interstage leakage flow (2). This is shown for the design condition in Fig. 13a ( $\beta_{in} = -0.27$ ), with mass flows normalised with respect to the annulus mass flow. With increasing superposed flow rate, the interstage leakage marginally increases (due to a slightly larger pressure drop across the rotor fins), but the net ingestion reduces significantly, which is also evidenced by the low ingestion from the gas concentration measurements in Fig. 11. The effect of  $\beta_{in}$  on the net ingestion is shown in Fig. 13b. For a given  $\lambda_T$  (i.e. a fixed superposed mass flow rate), the net ingestion increases with a more negative  $\beta_{in}$ . It has been demonstrated using gas concentration measurements that the ingress also increases with reducing  $\beta_{in}$  (Fig. 12). This can be explained by the shear argument from the turbulent transport model in Eq. 11. As the difference between the swirl in the annulus and the rotor becomes greater, stronger mixing will result in a greater transfer of mass into the cavity. Although the net ingestion does not vary with  $\beta_{in}$  when  $\lambda_T = 0$ , this does not mean that ingress is constant. Indeed, it is possible that ingress and egress increase at the same rate.

The radial component of velocity from the five-hole probe is an additional indicator for the change in ingestion. This is shown in Fig. 14 for the design condition, together with the axial and tangential velocity components. The velocity is normalised with respect to the maximum velocity magnitude for each case. A positive radial velocity relates to radially outward flow and vice versa. With the addition of superposed flows, the inward radial velocity component reduces, which is suggestive of lower ingestion. An area integral of velocity will give the convective mass flow. Mass transfer by diffusion is separately accounted for by the turbulent transport model.

## 6 Conclusions

The flow field, windage torque and ingestion characteristics of a low-pressure turbine stator-well cavity have been measured and computed. An engine-representative geometry was used with superposed flows entering the cavity, which modelled the leakage and coolant. The numerical results have been validated at experimental conditions and have provided insight into the fluid dynamic behaviour within the cavity. The experimental results are the first to relate simultaneous torque and cavity swirl measurements.

The computed and measured swirl revealed complex flow structures in the cavity, with the ingress path through both wheel-spaces determined by pairs of contra-rotating vortices. The addition of leakage and coolant significantly altered the upstream flow structures, but only weakly affected those in the downstream wheel-space, which behaved more like

**Fig. 13** Upstream net ingestion—a determination of different flow paths and b effect of  $\beta_{in}$  on the net ingestion (PR=1.24)

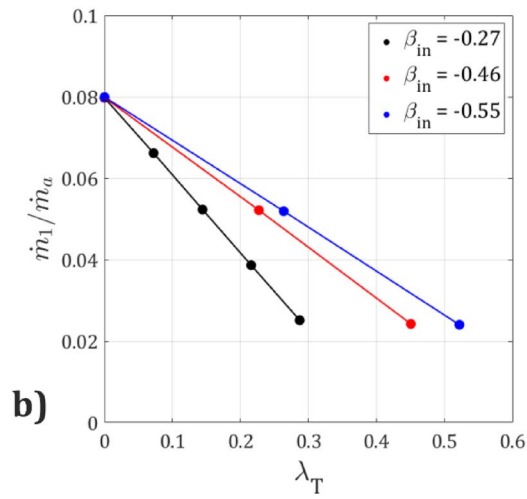
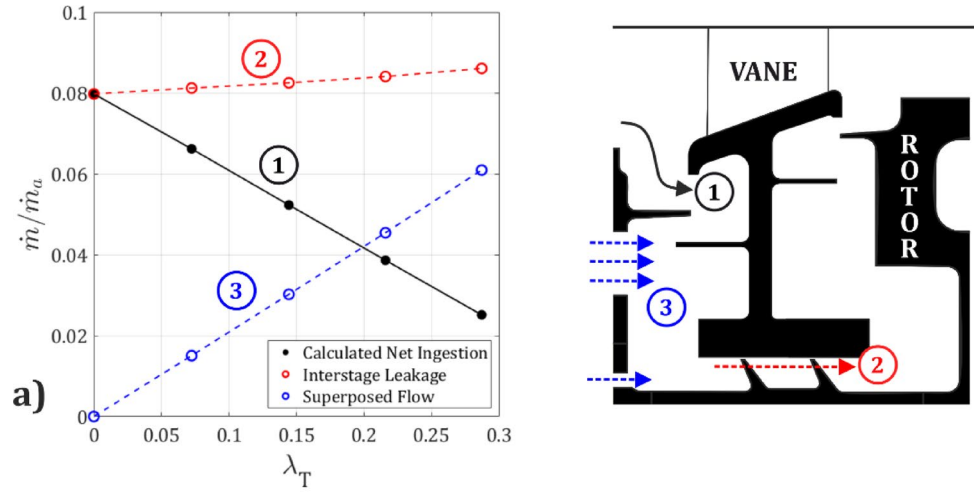
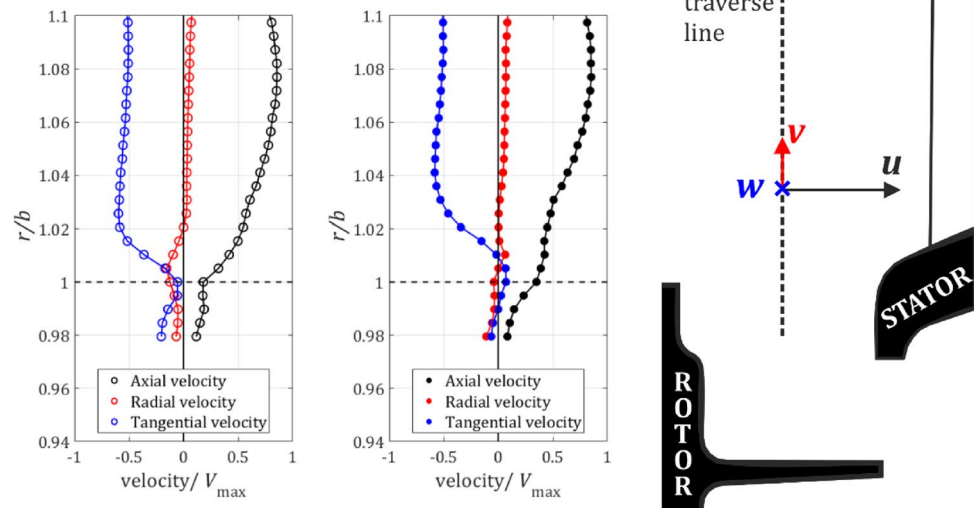


**Fig. 14** Velocity components at inlet to upstream wheel-space. Left:  $\lambda T=0$ , middle:  $\lambda T=0.29$  (PR=1.24;  $\beta_{in} = -0.27$ ;  $Re\Phi = 1.2 \times 10^6$ )



a classic rotor–stator system with a bore flow (interstage leakage) entering at low radius.

At the design condition with superposed flow (PR = 1.24;  $\beta_{in} = -0.27$ ;  $Re_\phi = 1.2 \times 10^6$ ;  $\lambda_T = 0.29$ ), the cavity windage torque reduced by 60% of that of the reference case ( $\lambda_T = 0$ ), directly caused by an increase in the swirl in the cavity. The swirl increase was due to a combined effect of the pre-swirled superposed flows and a reduction in the ingestion of annulus air. This improved sealing effectiveness was evidenced by gas concentration measurement/simulations and a reduced radial flow velocity into the cavity.

The change in windage moment coefficient relative to the reference case,  $\Delta C_M$ , was found to be strongly influenced by  $\beta_{in}$ , which directly affects the cavity swirl. Larger reductions in  $\Delta C_M$  were measured at a more negative  $\beta_{in}$  (fixed  $\lambda_T$ ), owing to a greater potential for windage reduction as the incoming swirl is against the rotational direction of the disc. A turbulent transport model was used to explain that the increased ingestion with more negative  $\beta_{in}$  was likely caused by a larger difference in swirl between the annulus and cavity, resulting in shear-driven diffusion.

Gas concentration and windage torque measurements revealed that the flow structure and windage moment coefficient was only weakly affected by PR and  $Re_\phi$ . In principle, and within the limits of dimensional similitude, the results could be scaled to a geometrically similar engine operating at the same fluid-dynamic conditions, providing practical insight to the engine designer. The effectiveness measurements can also be used by the designer to validate thermo-mechanical models that predict disc metal temperatures and heat transfer behaviour.

### Appendix 1

#### Example torque measurement

Figure 15 presents an example torque trace over time. The colour of each data point corresponds to a different superposed flow rate, as shown in the inset figure. After each flow rate, the superposed flows are set to zero and the reference case is collected. The repeatability of the reference case is within  $\pm 0.02$  Nm. Figure 15 also demonstrates the sensitivity of the torque meter to small changes in  $\lambda_T$ . Note that  $M$  is the measured torque: to find the change in windage torque caused by  $\lambda_T$ , the onboarding torque ( $M_{onboard}$ ) and reference torque ( $M_{ref}$ ) are first subtracted from  $M$ , as stated by Eqs. 6 and 7.

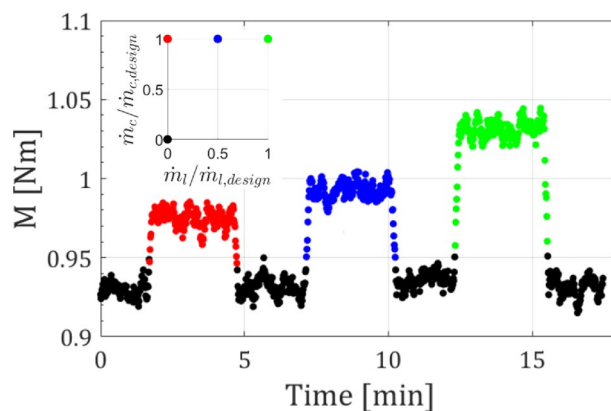


Fig. 15 Example torque trace over time with varying superposed flow rates

### Appendix 2

#### Calibration of interstage seal mass flow

The mass flow rate through the interstage seal was calibrated using the set-up presented in Fig. 16a. Here, the pipes into the annulus were blocked and a seal was attached to the stator rim downstream of the vane. This ensured that air entering the cavity via the superposed feed lines passed over the seal. Figure 16b shows the variation of mass flow with pressure drop across the seal, measured at the two locations highlighted in Fig. 16a. The seal mass flow is normalised with respect to the design condition (specified in Table 1). The relationship between mass flow and pressure ratio is independent over the range of  $Re_\phi$  tested in the experimental campaign. The derived interstage mass flow at the design condition ( $\dot{m}_f = \dot{m}_{f,d}$ ) is very close to the original design target and that which was predicted by computations, as shown by the two data points in Fig. 16b Tables 2, 3, 4.

### Appendix 3

#### Uncertainty analysis

The swirl ratio measured in the wheel-space is defined as:

$$\beta = \sqrt{\frac{(p_{total} - p_{static})RT}{0.5(p_{baro} + p_{static})\Omega^2 b^2}} \tag{13}$$

Ignoring any geometric uncertainties, the relative uncertainty is calculated as:

**Fig. 16** **a** Set-up of mass flow calibration across interstage seal and **b** calibration of mass flow with pressure drop at two  $Re\Phi$  conditions

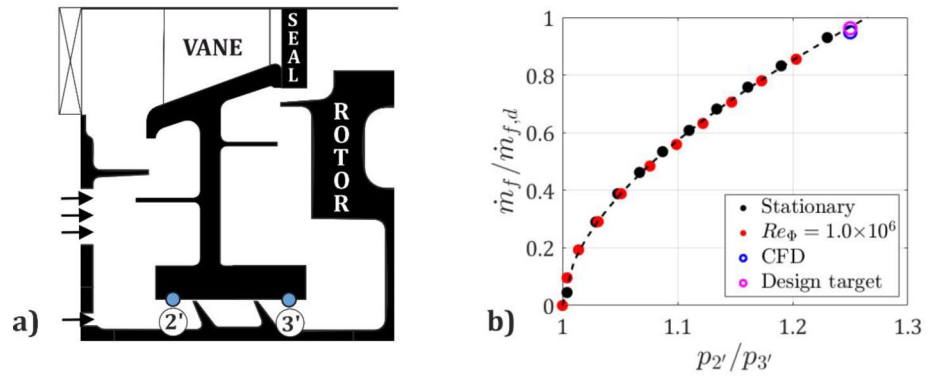


**Table 2** Instrumentation accuracy

$X_i$	$\delta X_i$	Range
$p_{baro}$	$\pm 1$ mbar	954–1073 mbar
$p_{upstream}$	$\pm 0.3\%$ FS	0–400 mbar
$p_{downstream}$	$\pm 0.3\%$ FS	–30–30 mbar
$T$	$\pm 0.5$ °c	10–30 °c
$\Omega$	$\pm 1$ rpm	0–6000 rpm

**Table 3** Upstream values for Fig. 7a

$r/b$	$\beta$	$\frac{\delta\beta}{\beta}$
0.971	–0.0786	1.90%
0.936	–0.153	1.90%
0.920	–0.129	1.90%
0.840	0.0786	1.90%
0.810	0	1.90%

**Table 4** Downstream values for Fig. 7a

$r/b$	$\beta$	$\frac{\delta\beta}{\beta}$
0.992	0.243	2.51%
0.946	0.196	2.24%
0.924	0.217	2.25%
0.902	0.199	2.23%
0.881	0.232	2.24%
0.837	0.216	2.28%
0.810	0.221	3.58%
0.790	0.172	3.03%

$$\left(\frac{\delta\beta}{\beta}\right)^2 = \frac{(0.5\delta p_{tot})^2 + (0.5\delta p_{static})^2}{(p_{tot} - p_{static})^2} + \left(\frac{0.5\delta T}{T}\right)^2 + \frac{(0.5\delta p_{baro})^2 + (0.5\delta p_{static})^2}{(p_{baro} + p_{static})^2} + \left(\frac{\delta\Omega}{\Omega}\right)^2 \quad (14)$$

**Acknowledgements** The authors thank Matt Hawthorne at Added Scientific Ltd for his support in this project. The doublets were printed by Laser Prototypes Europe Ltd with support on design for manufacture by Added Scientific. The calculations were performed using the University of Nottingham HPC Facility and Sulis at HPC Midlands Plus, which was funded by EPSRC grant EP/T022108/1.

**Author contributions** RWJ conducted the experiments and analysis, prepared the figures and wrote the original draft. JAS and CMS designed the experimental rig and methodology. ZL and LC carried out the computational analysis, supervised by RJL and SA. GDL reviewed and edited the paper and managed the project.

**Funding** This project was funded by Clean Sky 2 Joint Undertaking under the European Union’s Horizon 2020 research and innovation program (H2020-GAP-886112-ACUHRA).

**Availability of data and materials** Supporting data can be made available to bona fide researchers. Details of how to request access are available at the University of Bath data archive (<http://dx.doi.org/10.15125/BATH-00116>).

**Declarations**

**Conflict of interest** The authors declare there are no competing interests associated with this work.

**Ethical Approval** None.

**Open Access** This article is licensed under a Creative Commons Attribution 4.0 International License, which permits use, sharing, adaptation, distribution and reproduction in any medium or format, as long as you give appropriate credit to the original author(s) and the source, provide a link to the Creative Commons licence, and indicate if changes were made. The images or other third party material in this article are included in the article's Creative Commons licence, unless indicated otherwise in a credit line to the material. If material is not included in the article's Creative Commons licence and your intended use is not permitted by statutory regulation or exceeds the permitted use, you will need to obtain permission directly from the copyright holder. To view a copy of this licence, visit <http://creativecommons.org/licenses/by/4.0/>.

**References**

Andreini A, Da Soghe R, Facchini B, Zecchi S (2008) Turbine stator well cfd studies: effects of cavity cooling air flow. In: Proceedings of the ASME Turbo Expo 2008. ASME Paper No. GT2008–51067

- Andreini A, Da Soghe R, Facchini B (2011) Turbine stator well cfd studies: effects of coolant supply geometry on cavity sealing performance. *ASME J Turbomach* 133(2):021008
- Barsi D, Lengani D, Simoni D, Venturino G, Bertini F, Giovannini M, Rubecchini F (2022) Analysis of the loss production mechanism due to cavity-main flow interaction in a low-pressure turbine stage. *ASME J Turbomach* 144(9):091004
- Coren DD, Atkins NR, Long CA, Eastwood D, Childs PRN, Guijarro-Valencia A, Dixon JA (2011) The influence of turbine stator well coolant flow rate and passage configuration on cooling effectiveness. In: *Proceedings of the ASME Turbo Expo 2011*. ASME Paper No. GT2011-46448
- Coren DD, Atkins NR, Turner JR, Eastwood DE, Davies S, Child PRN, Dixon JA, Scanlon TJ (2013) An advanced multiconfiguration stator well cooling test facility. *ASME J Turbomach* 135(1):011003
- Eastwood D, Coren DD, Long CA, Atkins NR, Childs PRN, Scanlon TJ, Guijarro-Valencia A (2012) Experimental investigation of turbine stator well rim seal, re-ingestion and interstage seal flows using gas concentration techniques and displacement measurements. *ASME J Eng Gas Turb Power* 134(8):082501
- Fitzpatrick JN (2013) Coupled thermal-fluid analysis with flowpath-cavity interaction in a gas turbine engine. Purdue University. Master's Thesis
- Gier J, Stubert B, Brouillet B, De Vito L (2005) Interaction of shroud leakage flow and main flow in a three-stage lp turbine. *ASME J Turbomach* 127(4):649-658
- Graikos D, Tang H, Sangan CM, Lock GD, Scobie JA (2022) A new interpretation of hot gas ingress through turbine rim seals influenced by mainstream annulus swirl. *ASME J Eng Gas Turb Power* 144(11):111005
- Guida R, Lengani D, Simoni D, Ubaldi M, Zunino P (2018) New facility setup for the investigation of cooling flow, viscous and rotational effects on the interstage seal flow behavior of a gas turbine. In: *Proceedings of the ASME Turbo Expo 2018*. ASME Paper No. GT2018-75630
- Hunter SD, Manwaring SR (2000) Endwall cavity flow effects on gas-path aerodynamics in an axial flow turbine: part i—experimental and numerical investigation. In: *Proceedings of the ASME Turbo Expo 2000*. ASME Paper No. 2000-GT-651
- Jackson R, Lock GD, Sangan CM, Scobie JA, Li Z, Christodoulou L, Jefferson-Loveday R, Ambrose S (2023) Windage reduction in low pressure turbine cavities. part 2: experimental and numerical results. In: *Proceedings of the ASME Turbo Expo 2023*. ASME Paper No. GT2023-102311
- Kader B (1981) Temperature and concentration profiles in fully turbulent boundary layers. *Int J Heat Mass Transfer* 24(9):1541-1544
- Kármán Th, von. (1921) Über luminare und turbulente reibung. *Zeitschrift Für Angewandte Mathematik Mechanik* 1:233-252
- Liu H, An Y, Zou Z (2014) Aerothermal analysis of a turbine with rim seal cavity. In: *Proceedings of the ASME Turbo Expo 2014*. ASME Paper No. GT2014-25276
- Li Z, Christodoulou L, Jefferson-Loveday R, Ambrose S, Jackson R, Lock GD, Sangan CM, Scobie JA (2023) Windage reduction in low pressure turbine cavities. part 1: flow control concept design using numerical modelling. In: *Proceedings of the ASME Turbo Expo 2023*. ASME Paper No. GT2023-103532
- Owen JM, Rogers RH (1989) Flow and heat transfer in rotating-disc systems, volume 1—rotor stator systems. Research Studies Press Ltd, Taunton
- Savov SS, Atkins NR (2017) A rim seal ingress model based on turbulent transport. In: *Proceedings of the ASME Turbo Expo 2017*. ASME Paper No. GT2017-63531
- Savov SS, Atkins NR, Uchida S (2017) A comparison of single and double lip rim seal geometries. *ASME J Eng Gas Turb Power* 139(11):112601
- Schrewe S, Werschnik H, Schiffer HP (2013) Experimental analysis of the interaction between rim seal and main annulus flow in a low pressure two stage axial turbine. *ASME J Turbomach* 135(5):051003
- Valencia AG, Dixon JA, Da Soghe R, Facchini B, Smith PE, Muñoz J, Eastwood D, Long CA, Coren DD, Atkins NR (2012) An investigation into numerical analysis alternatives for predicting re-ingestion in turbine disc rim cavities. In: *Proceedings of the ASME Turbo Expo 2012*. ASME Paper No. GT2012-68592
- Zhang F, Wang X, Li J, Zheng D (2017) Numerical investigation on the effect of radial location of sealing air inlet and its geometry on the sealing performance of a stator-well cavity. *Int J Heat Mass Transfer* 115:820-832